Journal of Hydrology 529 (2015) 723–736

Contents lists available at ScienceDirect

Journal of Hydrology

journal homepage: www.elsevier.com/locate/jhydrol

A radiation-derived temperature-index snow routine for the GSSHA hydrologic model

Michael L. Follum [a,b,*], Charles W. Downer [a], Jeffrey D. Niemann [b], Spencer M. Roylance [c], Carrie M. Vuyovich [d]

[a] Hydrologic Systems Branch, Coastal and Hydraulics Laboratory, Engineer Research and Development Center, 3909 Halls Ferry Road, Vicksburg, MS 39180, USA
[b] Department of Civil Engineering, Colorado State University, Campus Delivery 1372, Fort Collins, CO 80523, USA
[c] Wilmington District, U.S. Army Corps of Engineers, 69 Darlington Avenue, Wilmington, NC 28403, USA
[d] Cold Regions Research and Engineering Laboratory, Engineer Research and Development Center, 72 Lyme Road, Hanover, NH 03755, USA

ARTICLE INFO

Article history:
Received 8 May 2015
Received in revised form 11 August 2015
Accepted 20 August 2015
Available online 29 August 2015
This manuscript was handled by
Konstantine P. Georgakakos, Editor-in-Chief

Keywords:
Spatial snow simulation
Spatially-distributed watershed model
Radiation-derived temperature-index snow model
Topographic effects on snow

SUMMARY

Accurate estimation of snowpack is vital in many parts of the world for both water management and flood prediction. Temperature-index (TI) snowmelt models are commonly used for this purpose due to their simplicity and low data requirements. Although TI models work well within lumped watershed models, their reliance on air temperature (and potentially an assumed lapse rate) as the only external driver of snowmelt limits their ability to accurately simulate the spatial distribution of snowpack and thus the timing of snowmelt. This limitation significantly reduces the utility of the TI approach in distributed hydrologic models because spatial variability within the watershed, including snowpack and snowmelt, is usually the primary reason for selecting a distributed model. In this paper, a new radiation-derived temperature index (RTI) approach is presented that uses a spatially-varying proxy temperature in place of air temperature within the TI model of the fully-distributed Gridded Surface Subsurface Hydrologic Analysis (GSSHA) watershed model. The RTI is derived from a radiation balance and includes spatial heterogeneity in both shortwave and longwave radiation. Thus, the RTI accounts for more local variation in the available energy than air temperature alone. The RTI model in GSSHA is tested at the Senator Beck basin in southwestern Colorado where observations for snow water equivalent (SWE) and LandSat-derived images of snow cover area (SCA) are available. The TI and RTI approaches produce similar SWE estimates at two non-forested and relatively flat sites with SWE observations. However, the two models can produce very different SWE values at sites with forests or topographic slopes, which leads to significant differences in the basin-wide SWE values of the two models. Furthermore, the RTI model provides better basin-wide SCA estimates than the TI model in 75% of the LandSat images analyzed.

Published by Elsevier B.V.

1. Introduction

Snow accumulation and ablation are important hydrologic processes in the western United States as well as many other regions of the world. For example, Barros and Lettenmaier (1993) estimated that snowmelt from headwater catchments that compose less than 25% of the total land area provide approximately 70% of the annual runoff in the western United States. Wahl (1992) estimated runoff from snowmelt contributes 50% to 80% of the annual downstream water supply. While the volume of water held within the snowpack is important, the timing of the release of water from the snowpack is also important for flood protection as well as agricultural and municipal water supplies. Furthermore, accurate estimation of the spatial pattern of snowpack is vital to determining the seasonal volume of snow water equivalent (SWE) and the shape, peak, and duration of the basin outflow due to snowmelt (Luce et al., 1998; Pomeroy et al., 2009).

Snow accumulation and melt are both driven by the fundamental laws of conservation of mass and energy. As described in Aguado (1985), the majority of studies indicate that net radiation is the primary source of energy for snowmelt, while turbulent heat transfer is of secondary importance. Spatial variations in net radiation due to cloud cover (Aguado, 1985; Sicart et al., 2006), sun position, topography (Blöschl et al., 1991; Kirnbauer et al., 1994), and vegetation result in heterogeneous snow accumulation and melt patterns throughout a basin. For example, Jost et al. (2007)

* Corresponding author at: Hydrologic Systems Branch, Coastal and Hydraulics Laboratory, Engineer Research and Development Center, 3909 Halls Ferry Road, Vicksburg, MS 39180, USA. Tel.: +1 (601) 634 2639.
E-mail address: Michael.L.Follum@usace.army.mil (M.L. Follum).

http://dx.doi.org/10.1016/j.jhydrol.2015.08.044
0022-1694/Published by Elsevier B.V.

found that elevation, forest cover, and aspect explain most of the large-scale variability in snowpack within a watershed in the Kootenay Mountains in southeastern British Columbia, Canada. Adequately simulating the accumulation and ablation processes within snow models, including spatial variability (e.g. forested and non-forested), is currently of much interest, as evidenced by the Snow Model Intercomparison Projects (SnowMIP 1 and 2) (Etchevers et al., 2004; Essery et al., 2009).

Water managers, hydrologists, and engineers commonly utilize numerical models to estimate the volume of SWE in headwater areas in order to plan for operations of reservoirs and other water control structures. One such model is the Gridded Surface Subsurface Hydrologic Analysis (GSSHA) model (Downer and Ogden, 2004), which has been widely-used for various military, civilian, and research applications (Downer et al., 2006; Sharif et al., 2010; Wright et al., 2014). GSSHA is a fully-distributed hydrologic model that simulates physically-based equations of mass and energy conservation on a structured grid. For snowpack simulation, the model can utilize either an energy-balance or a temperature-index (TI) method (Follum and Downer, 2013), with the TI model being based upon *SNOW-17* (Anderson, 1973, 2006). Energy-balance approaches can outperform TI models in representing the spatial heterogeneity of the snowpack (Kumar et al., 2013), but suffer from the need for highly-accurate forcing data (Lei et al., 2007) that are not available in most watersheds. Large-scale energy balance models, such as the National Weather Service's Snow Data Assimilation (SNODAS) model (Carroll et al., 2001; Barrett, 2003), simulate snow over the coterminous United States but do so at a 1 km^2 spatial resolution, which is coarser than the resolution used in many distributed hydrologic models. TI models are advantageous when forcing data are limited because they require only precipitation and air temperature data as drivers.

TI snow models have long been used within hydrologic models due to their simplicity of relating air temperature to snowmelt through the use of a melt factor. In these models, air temperature is used as an index (i.e. proxy) to determine the energy exchange across the snow-air interface (Anderson, 2006), where air temperature is typically estimated throughout the basin based on the local topographic elevation and a specified lapse rate. The use of TI models within fully-distributed models has increased due to the availability of air temperature data and gridded elevation data (Daly et al., 2000; Zeinivand and De Smedt, 2009; Jost et al., 2012; Kumar et al., 2013). However, TI approaches typically do not account for the effects of slope, aspect, and vegetation cover, which have been shown to control snowpack and snowmelt patterns. It has also led to inaccuracies when comparing simulated snowpack to satellite-derived estimates of snow cover area (SCA), which are often the only validation dataset available (Mhawej et al., 2014; Vuyovich and Jacobs, 2011).

More recently, methods have been utilized to better account for topographic and vegetative differences within TI models (Hock (2003) provides a thorough overview). Simple approaches, such as empirically adjusting the temperature based on aspect and the location of forested areas, have had some success (Kang, 2005). Other approaches use a melt factor that varies based on monthly (Cazorzi and Fontana, 1996; Dunn and Colohan, 1999) or hourly (Hock, 1999) radiation calculations over the discretized area. Shamir and Georgakakos (2006) modified melt factors based on the aspect of each cell in the model domain to simulate a distributed snowpack using a TI model. Another common method (Brubaker et al., 1996; Bookhagen and Burbank, 2010; Kustas et al., 1994; Molotch and Bales, 2006) is to separate the drivers of melt into two terms. The first term estimates the melt due to turbulent heat flux based on the melt factor and air temperature. The second term converts a radiation amount to an amount of melt. In this approach, the melt factor is only used to estimate melt due to turbulent heat flux instead of the total melt. Butcher (2009) incorporated this method into the *SNOW-17* model (producing *SNOW-17 EB*) but found that *SNOW-17* outperformed *SNOW-17 EB* when deployed at the Reynolds Creek Experimental Watershed in Idaho, USA. This result likely occurs because *SNOW-17 EB* requires high-quality spatiotemporal forcing data (e.g., temperature, precipitation, cloud cover, relative humidity, shortwave radiation, longwave radiation), which is an issue shared by full energy-balance snow models (Franz et al., 2008).

The objective of this paper is to better account for spatial heterogeneity of available energy within the GSSHA TI model while preserving the strengths of this approach, particularly its limited data requirements and widely-used mathematical structure. In TI models, air temperature is used as a proxy for the energy available for heating or melting the snowpack. This approach is relatively successful due to the high correlation between air temperature and energy balance components (Ohmura, 2001). In this paper, we propose an alternative proxy temperature that is derived from the radiation balance including simple calculations of the net shortwave radiation (which includes the effects of topography, clouds, vegetation, and albedo) and net longwave radiation (which includes contributions from the air, vegetation, cloud cover, and approximate snow temperature). This radiation-derived temperature index (RTI) approach is explored because radiation is typically the primary driver of snowmelt in many locations, data are available to incorporate spatial variations in the components of the radiation balance (and thus the RTI), and this approach retains the widely-used TI model structure.

2. Methodology

2.1. Existing GSSHA TI model

The existing TI model in GSSHA (from now on, referred to as TI) is based on *SNOW-17* (Anderson, 1973, 2006) and was implemented into GSSHA by Follum and Downer (2013). *SNOW-17* is typically operated by the National Weather Service using a time step (dt) of 6 h but can be used at various time intervals (Anderson, 2006). GSSHA allows for a variable time step for various processes (e.g., flow routing, infiltration, and evaporation), but it uses an hourly time step for snow simulation. In the TI model, precipitation (P) in each cell is considered to fall as snow when $T_a \leqslant$ PXTEMP, where T_a is the air temperature (°C) and PXTEMP is the temperature (°C) at which precipitation is considered snow. An under-catch adjustment factor (SCF) can be used to account for inaccuracies in precipitation data (Anderson, 2006). Each cell of the GSSHA model can have varying values of T_a and P, and therefore each cell can accumulate and melt snow independently from the surrounding cells.

The change in heat deficit (ΔD_t, mm of SWE) within the snowpack due to differences between the temperature of the air and snow surface is accounted for as:

$$\Delta D_t = \mathrm{NMF} \cdot (\mathrm{ATI} - T_{sur}) \tag{1}$$

where ATI is the antecedent temperature index (°C) (as calculated in Anderson (2006)), T_{sur} is the snow surface temperature (as in Anderson (2006), T_{sur} is assumed to be equal to T_a or 0 °C, whichever is less), and NMF is the negative melt factor (mm °C^{-1} dt^{-1}). NMF is calculated as:

$$\mathrm{NMF} = \mathrm{NMF}_{max} \cdot (dt/6) \cdot (M_f/M_{f,max}) \tag{2}$$

where NMF_{max} is the maximum negative melt factor (mm °C^{-1} (6 h)$^{-1}$), M_f is the melt factor (mm °C^{-1} dt^{-1}), and $M_{f,max}$ is the maximum melt factor (mm °C^{-1} (6 h)$^{-1}$), which is usually calibrated. An additional calibration parameter, TIPM, is included in

the calculation of ATI and ranges between 0.0 and 1.0 (Anderson, 2006). The change in heat deficit due to snowfall is also accounted for within the TI model using the approach from Anderson (2006).

Melt occurs once the energy input into the snowpack overcomes the heat deficit. When little or no rain occurs (less than 1.5 mm during the previous 6 h), the amount of melt in a time step is calculated as:

$$M = [M_f \cdot (T_a - \text{MBASE}) + 0.0125 \cdot P \cdot f_r \cdot T_r] \cdot dt \quad (3)$$

where M is the melt in mm, P is in mm, MBASE is the temperature above which snow begins to melt (typically set to 0 °C), f_r is the fraction of precipitation in the form of rain when $T_a > 0$ °C, and T_r is the precipitation temperature in °C (taken as equal to T_a or 0 °C, whichever is greater). The melt factor is calculated as:

$$M_f = (dt/6) \cdot [S_v \cdot A_v \cdot (M_{f,max} - M_{f,min}) + M_{f,min}] \quad (4)$$

where S_v is a sine curve that accounts for seasonal melt variation, A_v is a seasonal melt variation adjustment (for the Northern Hemisphere, it is set to 1.0 when lower than 54°N latitude, and it varies linearly between 0.0 and 1.0 as a function of time of year when above 54°N latitude), and $M_{f,min}$ is a calibrated minimum melt factor (mm °C^{-1} (6 h)$^{-1}$). Using S_v and A_v, the model varies M_f seasonally between $M_{f,min}$ and $M_{f,max}$, which empirically accounts for the seasonal variations in solar radiation and snow albedo.

When at least 1.5 mm of rainfall occurs during the previous 6 h an energy balance is used to calculate the amount of snowmelt with the assumption that snow surface temperature is 0 °C, incoming solar radiation is negligible, and incoming longwave radiation is equal to black body radiation (Anderson, 2006):

$$M = \sigma \cdot dt \cdot [(T_a + 273)^4 - 273^4] + 0.0125 \cdot P \cdot f_r \cdot T_r + 8.5 \cdot f_u \cdot (dt/6) \cdot [(\text{rh} \cdot e_{sat} - 6.11) + 0.00057 \cdot P_a \cdot T_a] \quad (5)$$

where σ is the Stefan–Boltzmann Constant ($6.12 \cdot 10^{-10}$ mm K^{-1} h^{-1}), f_u is the average wind function (mm mb^{-1} (6 h)$^{-1}$), rh is the relative humidity (assumed to be 0.9 during rain-on-snow events) (Anderson, 1973, 2006), P_a is atmospheric pressure (mb, calculated based on elevation) (Anderson, 2006), and e_{sat} is the saturated vapor pressure (mb, calculated based on Smith, 1993). Water leaves the snowpack when the liquid water content exceeds the liquid holding capacity, which is calculated as a calibrated percentage (PLWHC) of the ice portion of the snow cover (Anderson, 2006).

2.2. New GSSHA RTI model

In the RTI model, a radiation-derived temperature (T_{rad}, °C) replaces T_a in the equations that are used to calculate snowmelt (Eqs. (3) and (5)), while rainfall and snowfall continue to be distinguished using T_a. T_{rad} is calculated based on a radiation balance at the surface of the snowpack. If one neglects all terms in the snow surface energy balance aside from radiation, one can write:

$$\text{LW}_{\uparrow} = \text{SW}_{\downarrow,net} + \text{LW}_{\downarrow} \quad (6)$$

where $\text{LW}_{\uparrow}$ is outgoing longwave radiation, $\text{SW}_{\downarrow,net}$ is the net shortwave radiation, and $\text{LW}_{\downarrow}$ is the downwelling longwave radiation. Eq. (6) neglects any advected heat from precipitation, ground heat flux, sensible heat flux, latent heat flux, heat lost from melt water leaving the snowpack, or changes in the thermal energy of the snowpack (i.e. heat deficit). Using the Stefan–Boltzmann Law to relate the radiated energy to temperature, one can calculate an estimate of the snow surface temperature, which is T_{rad} (°C), as:

$$T_{rad} = \left[\frac{\text{LW}_{\downarrow} + \text{SW}_{\downarrow,net}}{\varepsilon_{snow}\sigma}\right]^{1/4} - 273.15 \quad (7)$$

where all radiation terms are in units of W m^{-2}, ε_{snow} is the emissivity of snow (assumed to be 1.0), and σ is the Stefan–Boltzmann constant (approximated as $5.6704 \cdot 10^{-8}$ W m^{-2} K^{-4}). T_{rad} is not expected to represent the actual temperature of the snow surface because of the assumptions described earlier. In addition, the calculation of T_{rad} does not consider the ice/water phase transition, so T_{rad} can exceed 0 °C. Instead, T_{rad} is interpreted as an index of energy that is available to heat or melt the snowpack. Although it is simplistic, this approach considers more elements of the energy balance than the TI model. T_a in the TI model is only directly associated with the downwelling longwave radiation from the air ($\text{LW}_{\downarrow,air}$), which is a component of $\text{LW}_{\downarrow}$ ($\text{LW}_{\downarrow}$ includes longwave contributions from the air, canopy, and cloud cover). T_{rad} in the RTI model considers both $\text{SW}_{\downarrow,net}$ and $\text{LW}_{\downarrow}$ (Fig. 1).

Methods were selected to calculate $\text{SW}_{\downarrow,net}$ and $\text{LW}_{\downarrow}$ that introduce as few parameters and data requirements as possible. $\text{LW}_{\downarrow}$ is determined by first calculating the downwelling longwave radiation at the top of canopy ($\text{LW}_{\downarrow,toc}$), which includes longwave radiation from the air and clouds. Neglecting the impact of the surrounding terrain on $\text{LW}_{\downarrow}$, GSSHA (Downer and Ogden, 2006) uses methods developed and tested by TVA (1972) to estimate $\text{LW}_{\downarrow,toc}$ as:

$$\text{LW}_{\downarrow,toc} = \sigma\varepsilon_a(T_a + 273.15)^4 \cdot (1.0 + 0.17N^2) \quad (8)$$

where ε_a is the air emissivity, and N is the fractional cloud cover. Various methods are available for calculating ε_a (TVA, 1972; Idso, 1981; Prata, 1996), but they often require additional data such as relative humidity. To keep the forcing data requirements low, ε_a is estimated as 0.757 when snow is present (Bras, 1990). T_a is linearly adjusted for local variation in elevation based on Bras (1990):

$$T_a = T_g + \theta(\text{Elev}_g - \text{Elev}_c) \quad (9)$$

where T_g is the measured air temperature at a gage (°C), θ is a positive lapse rate (°C m^{-1}), and Elev_g and Elev_c are the elevations of the temperature gage and the cell of interest (m), respectively. Following the parsimonious approach of Liston and Elder (2006), the incident longwave radiation at the snow surface ($\text{LW}_{\downarrow}$) can then be estimated as:

$$\text{LW}_{\downarrow} = \text{LW}_{\downarrow,toc}(1 - F_c) + F_c\varepsilon_c\sigma(T_{canopy} + 273.15)^4 \quad (10)$$

where T_{canopy} is the canopy temperature (°C) (assumed equal to the air temperature following DeWalle and Rango, 2008), ε_c is the canopy emissivity (assumed equal to 1 following Sicart et al., 2004), and F_c is the fractional canopy cover, which is 0 if no forest is present. Otherwise, F_c is estimated as (Liston and Elder, 2006):

$$F_c = f_a + f_b \ln(\text{LAI}) \quad (11)$$

where f_a and f_b are set to 0.55 and 0.29, respectively (Pomeroy et al., 2002), and LAI is the leaf area index within the cell. LAI data are required for the RTI model but not the TI model. However, LAI is already used to estimate the canopy resistance for evapotranspiration calculations in GSSHA, so it is not a new data requirement for the model as a whole. Liston and Elder (2006) also provides a table of LAI values for tree types that are common in cold climates.

The amount of downwelling shortwave radiation that is absorbed by the snow surface is:

$$\text{SW}_{\downarrow,net} = (1 - \alpha)\text{SW}_{\downarrow} \quad (12)$$

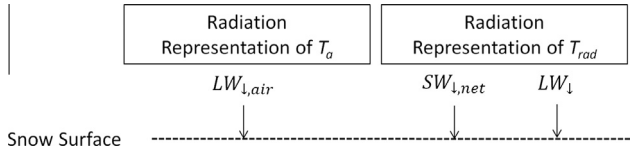

Fig. 1. Radiation components included in the proxy temperatures T_a and T_{rad}.

where $SW_{\downarrow}$ is the incident shortwave radiation and α is the albedo of the snowpack. Measurements of $SW_{\downarrow}$ are rarely available, and if available, they are typically from a single location. Therefore, $SW_{\downarrow}$ for each grid cell is estimated:

$$SW_{\downarrow} = S_0 K_r K_{atm} K_c K_v K_s K_t \quad (13)$$

where S_0 is the solar constant (1366 W m^{-2} from Liou, 2002) and the K factors are the reductions in the shortwave radiation due to distance from the earth to the sun (K_r), atmospheric scattering (K_{atm}), absorption by clouds (K_c), vegetation (K_v), slope/aspect of terrain (K_s), and topographic shading (K_t).

The adjustment K_r accounts for the effects of the distance from the sun based on the Julian day (JD) (TVA, 1972):

$$K_r = \left[1.0 + 0.017 \cos\left(\frac{2\pi}{365}(186 - \mathrm{JD})\right)\right]^{-2} \quad (14)$$

The reduction in shortwave radiation due to atmospheric thickness as well as aerosols and moisture (K_{atm}) is estimated for each cell based on its elevation (Allen et al., 2005):

$$K_{atm} = 0.75 + (2 \cdot 10^{-5}) \cdot \mathrm{Elev}_c \quad (15)$$

Other methods of calculating K_{atm} are available (e.g., Eagleson, 1970; Bras, 1990; Shuttleworth, 1993), but they require additional parameters or data. The reduction in shortwave radiation (K_c) due to absorption and reflection by clouds is determined as (TVA, 1972):

$$K_c = 1.0 - 0.65N^2 \quad (16)$$

where N is the fractional cloud cover. Other methods have been suggested for estimating the effects of clouds on $SW_{\downarrow}$ (see DeWalle and Rango, 2008), but the TVA (1972) method was selected to be consistent with the source used for calculation of $LW_{\downarrow}$.

The reduction in shortwave radiation reaching the ground surface due to vegetation (K_v) is set equal to the vegetation transmission coefficient, a parameter that is vegetation-type specific and represents a fraction of the shortwave radiation that is not intercepted by the vegetation canopy (see Bras, 1990). The vegetation transmission coefficient is a standard input for evaporation calculations within GSSHA, and has values ranging between 0 for complete canopy coverage and 1 for no canopy coverage.

The solar radiation emitted from the sun rarely strikes the land surface at a perpendicular angle, which results in a reduction (K_s) in the incident shortwave radiation per unit area. K_s can be calculated based on the angle of incidence (φ), which is the angle between the solar beam on the surface and a vector that is normal to that surface (Fig. 2). Duffie and Beckman (1980) calculate φ using the latitude, slope, and azimuth angle of the grid cell, and the solar declination (Shuttleworth, 1993) and hour (Duffie and Beckman, 1980) angles. K_s is then calculated as

$$K_s = \cos(\varphi) \quad (17)$$

Direct solar radiation can also be blocked by nearby topography, such as when mountains shade valleys. This effect is represented by K_t. Hourly values of solar azimuth (Duffie and Beckman, 1980) and solar elevation angles (Eagleson, 1970) are calculated and used in combination with geometry of the topography to determine if any cell within the simulation domain blocks the direct line between the solar location and the cell surface. If the sun is blocked during an hour, then K_t is set to 0.0 for that hour (indicating complete shading). Otherwise, K_t is set to 1.0 (indicating no shading). This approach is similar to that of the *GEOTOP* model (Zanotti et al., 2004).

Most equations used to calculate snow albedo (α) assume that α gradually declines over time and then suddenly increases when fresh snow falls on the snowpack. A summary of different methods used to calculate α can be found in DeWalle and Rango (2008).

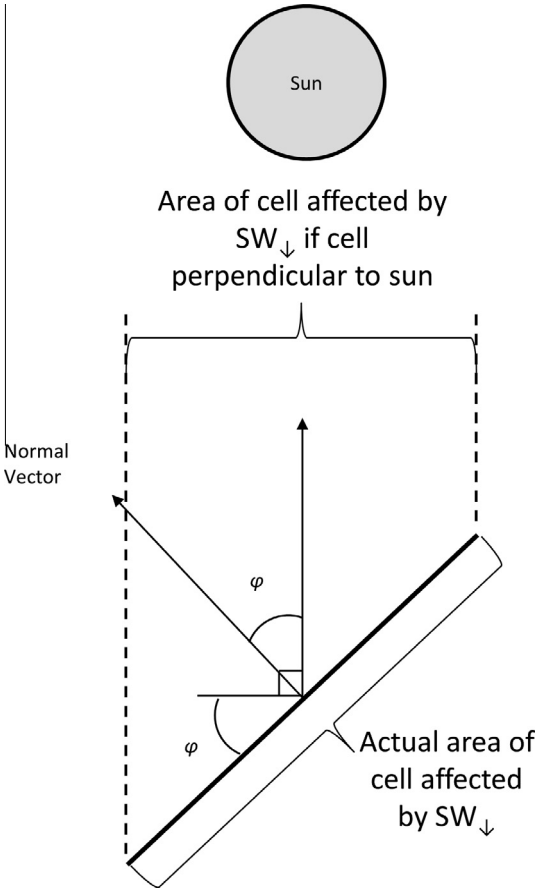

Fig. 2. Two-dimensional representation of the reduction in $SW_{\downarrow}$ due to the angle of incidence (φ) between the sun and the normal vector of the terrain. The TI model does not account for this reduction in $SW_{\downarrow}$. The RTI model calculates the reduction in three-dimensional space.

Here, daily values of snow albedo (α) are computed based on the number of days since the last snowfall (d) following Henneman and Stefan (1999). For periods when no melt is occurring, α for the current day (t) is:

$$\alpha_t = 0.83 - 0.011 \cdot d \quad (18)$$

When melt is occurring:

$$\alpha_t = \alpha_{t-1} - w \quad (19)$$

where w is 0.17 if the average daily temperature is above 0 °C, and 0.013 when it is not. The minimum allowed value for α is 0.38. This albedo model does not account for dust or other particulates, which can have important effects on snow ablation (Painter et al., 2007; Skiles et al., 2012, 2015). However, the RTI model can potentially include dust impacts in the future by adjusting α, whereas the TI model does not directly consider the albedo.

3. Model application

3.1. Study area

The TI and RTI snow models in GSSHA are tested at the 2.9 km^2 Senator Beck Basin (SBB) in southwestern Colorado. The study period is 1 July 2006 through 30 September 2012, which is approximately water year (WY) 2007 through WY 2012. The SBB is in the Ouray Ranger District of the Uncompahgre National Forest in the western San Juan Mountains (Fig. 3). It is located at 37° 54' 24.8″ N × 107° 43' 34.6″ W and has an elevation range from

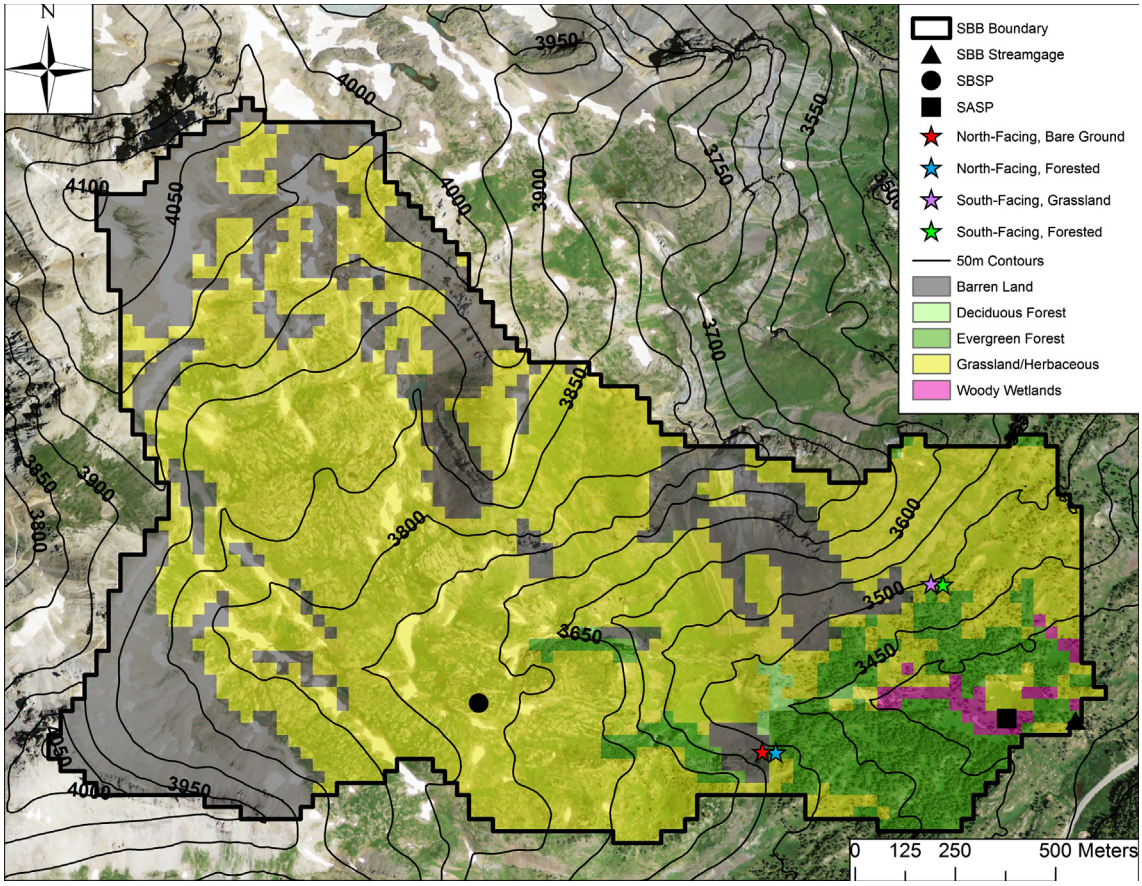

Fig. 3. SBB, Colorado, USA. Land cover classifications are from the 2006 National Land Cover Database and are overlain on United States Geological Survey 1-m orthoimagery data. Elevation contours (50 m) are from the 1/3-arc-second National Elevation Dataset. Sites considered in this study are shown by black symbols and colored stars. (For interpretation of the references to color in this figure legend, the reader is referred to the web version of this article.)

3362 m to 4118 m. The basin is primarily alpine terrain with bare rock and tundra as well as some forested areas below 3600 m. It is extensively gaged for both hydrometeorology and hydrology by the Center for Snow and Avalanche Studies. Additional basin information and data are provided by Landry et al. (2014).

The Swamp Angel Study Plot (SASP) and Senator Beck Study Plot (SBSP) are monitored within the basin. SASP has a lower elevation (3371 m) and is located in a large forest clearing with surrounding terrain that provides shelter from wind effects on precipitation and snowpack measurements. SBSP is a more-exposed and higher-elevation site (3714 m) that is located in alpine tundra where the effects of wind are more prevalent. Temperature, shortwave radiation, longwave radiation, and snow depth data are available for SASP and SBSP (Fig. 3), but precipitation data are only available for SASP.

The Center for Snow and Avalanche Studies uses formal snow cover profiles adjacent to the SASP and SBSP sites to measure SWE, snow depth, and snow density. Measurements are taken monthly in the early winter and weekly during the late winter and spring at SASP, and they are taken as feasible at SBSP. As discussed in Skiles et al. (2012), measurements of SWE are taken several meters away from the SBSP weather station and may not reflect the SWE exactly at the weather station site. Therefore, rather than using the SWE measurements from the snow cover profiles, the densities from the snow cover profiles are used with automated depth measurements at the SBSP weather station to determine more accurate SWE estimates at the SBSP weather station site itself (Skiles et al., 2012). For consistency, the same approach is used at SASP, but the differences are smaller at this site. These SWE estimates will be used throughout this study.

3.2. Additional comparative snow data

The SNow THERmal Model (SNTHERM; Jordan, 1991) was previously used to model the SWE at SASP and SBSP (Landry et al., 2014). Thus, the TI and RTI results can be compared to a multilayer energy-balance snow model, which is based on the mass and energy balance model by Anderson (1976). It should be noted, however, that the SNTHERM parameters were not calibrated but set to published values in those simulations.

To supplement the data from the SBSP and SASP sites, LandSat 5 imagery was used to derive snow cover area (SCA) maps of the basin. LandSat 5 includes six spectral bands (blue, green, red, near-infrared, and two shortwave infrared) at a 30 m resolution, which create unique spectral signatures that can be used in the mapping of snow cover within a basin (Dozier and Marks, 1987). The Iterative Self-Organizing Data Analysis Techniques (ISODATA) (Ball and Hall, 1965; Tou and Gonzalez, 1974) within the ERDAS (1999) software was used to group pixels with similar spectral signatures into thematic classes, which were then assigned a designation as snow, no-snow, or snow fringe based on the ISODATA thematic classes and visual interpretation of the classes compared to orthoimagery. Snow fringe was defined as the transition between the snow/no-snow classes and likely represents partial snow coverage within the pixel. In total, 32 LandSat images are available for the study period, but most images were collected when the snow cover was either absent or nearly complete, which greatly reduces their value for testing the models. Thus, only 12 images were used in the study, all of which indicate between 25% and 75% coverage of snow within the basin.

3.3. Model forcing data

The Watershed Modeling System (Aquaveo, 2013) was used to develop a 30-m structured grid for GSSHA. This resolution was judged to adequately capture the spatial heterogeneity of the basin while remaining computationally efficient. The basin was delineated using the 1/3-arc-second (~9 m) National Elevation Dataset (Gesch et al., 2002), and elevation data were then mapped onto the structured grid of the basin, which contains 3207 grid cells.

Land cover classifications were derived from the 2006 National Land Cover Database (Fry et al., 2011). Approximately 62.1% of the basin is classified as grass/herb, 27.2% as barren land, 9.4% as evergreen forest, 0.3% as deciduous forest, and 1.1% as wooded wetlands (Fig. 3). Comparisons between the land cover map and United States Geological Survey 1-m orthoimagery data (from 28 May 2014) show that the wooded wetlands are actually grass/herb and were therefore reclassified.

The precipitation data from SASP are assumed to apply to the entire SBB. Although the basin is relatively small, the topographic relief likely produces uncaptured variations in precipitation. The temperature data from SASP and SBSP were used to calculate hourly values of lapse rate, which was restricted to the range from 0.0 to 0.00981 °C m^{-1} to avoid occasional anomalous temperature patterns. Once the lapse rate was determined, the temperature for each grid cell was calculated relative to SBSP using Eq. (9). Cold air drainage from higher elevations into the sheltered terrain pocket at SASP does occur, which sometimes causes colder overnight low temperatures at SASP than SBSP (Landry et al., 2014). This negative lapse rate is assumed to be local to the SASP terrain pocket and not representative of the temperature profile throughout the majority of the basin and therefore neglected in the model. Satellite-derived and locally observed cloud cover data are available from the National Centers for Environmental Information (NCEI, https://www.ncdc.noaa.gov/). Observed cloud cover measurements, which vary in temporal resolution, are often taken at airports as part of the local climatological data archived at the NCEI. These surface aviation cloud cover data are available throughout the day and night from the Telluride Regional Airport (TEX), which is approximately 16 km to the northwest of SBB. This dataset consists of five classifications of cloud cover. Each classification is associated with a range of eighths (or oktas) of the sky that are covered by clouds (e.g., the scattered clouds classification ranges from 3 to 4 oktas). Based on the range of each classification, we determined cloud cover percentages as follows: clear (CLR) – 0%, few clouds (FEW) – 12.5%, scattered clouds (SCT) – 43.75%, broken sky (BKN) – 75%, and overcast (OVC) – 100%. When multiple classifications were recorded for the same time period the average of the associated percentages was used. The cloud cover was measured at irregular time intervals, but was interpolated to produce hourly data for this project. Cloud cover data are not available from 08 April 2009 through 11 November 2009, which provides an opportunity to investigate the importance of this data (recall that the TI model does not require cloud cover data, while the RTI model does). For this period, the cloud cover values were determined by randomly sampling the observations from the same day and hour during the other years in the dataset. This approach aims to capture realistic variations in cloud cover, but it is not expected to reproduce the actual cloud cover in 2009. The effects of this approach will be examined later.

3.4. Parameter estimation and calibration

The Model-Independent Parameter Estimation and Uncertainly Analysis (PEST) method (Doherty et al., 1994) was used to calibrate the parameters within the TI and RTI models. PEST is a nonlinear parameter estimator that calibrates numerous parameters simultaneously to produce the best fit between observed and simulated results. In this study, the TI and RTI models were calibrated to reproduce SCA, which characterizes the extent of snowpack across the watershed (not the SWE observations, which are available only at a few points). In particular, the error between the model and the observations is calculated:

$$\text{Error} = \frac{A_{over} + A_{under}}{A_{obs}} \tag{20}$$

where A_{over} is area where the model predicts snow cover but no snow is observed, A_{under} is the area where the model predicts no snow cover but snow is observed, and A_{obs} is the total observed SCA. An error value of 0 indicates perfect fit between simulated and observed SCA. In this comparison, cells that are classified as snow-fringe from the LandSat analysis are considered snow. The six LandSat SCA estimates from the first three water years (1 July 2006 through 30 September 2009) were used as the calibration period, and the remaining six SCA estimates from the last three water years were used as the validation period.

The allowable range, starting value, calibrated value, and sensitivity ranking of each parameter for the TI and RTI models are shown in Table 1. Precipitation and temperature data are expected to be accurate at SBB, therefore the SCF and MBASE parameters were assigned to their default values of 1.0 and 0 °C, respectively, and not calibrated. PXTEMP was also set to 0 °C. The lower limit of the calibration limit was set to 0.001 for all other parameters, with the starting value being approximately the average of the allowable range. The upper limit of the allowable range for TIPM was set based on physical ranges from Anderson (2006), while the upper limit for PLWHC was set to 0.1 based on typical values found in the field (Singh et al., 1997; Gerdel, 1954). The upper limits for $M_{f,min}$ and $M_{f,max}$ were set to double their approximate values within the conterminous United States from Anderson (2006). The physical range of K_v is between 0.0 and 1.0, but only K_v values for deciduous trees ($K_{v,deciduous}$) and evergreen trees ($K_{v,evergreen}$) are used as calibration parameters. The starting value for both

Table 1
Allowable range, starting value, and calibrated values for the TI and RTI model parameters using PEST. Dashes indicate parameters that are not required in the associated model. The sensitivity ranking for each parameter is shown in parentheses.

Parameter	Units	Allowable range	Starting value	TI	RTI
$M_{f,max}$	mm °C^{-1} (6 h)$^{-1}$	0.001–2.400	1.200	1.103 (1st)	–
$M_{f,min}$	mm °C^{-1} (6 h)$^{-1}$	0.001–0.800	0.400	0.800 (2nd)	–
M_f	mm °C^{-1} (6 h)$^{-1}$	0.001–2.400	0.800	–	0.469 (1st)
NMF_{max}	mm °C^{-1} (6 h)$^{-1}$	0.001–2.400	1.200	1.794 (5th)	2.215 (3rd)
f_u	mm mb^{-1} (6 h)$^{-1}$	0.001–1.000	0.500	0.500 (6th)	0.500 (5th)
TIPM	Fraction	0.001–1.000	0.500	1.000 (3rd)	0.100 (2nd)
PLWHC	Fraction	0.001–0.100	0.050	0.033 (4th)	0.050 (5th)
$K_{v,deciduous}$	Fraction	0.001–1.000	0.400	–	0.400 (5th)
$K_{v,evergreen}$	Fraction	0.001–1.000	0.400	–	1.000 (4th)

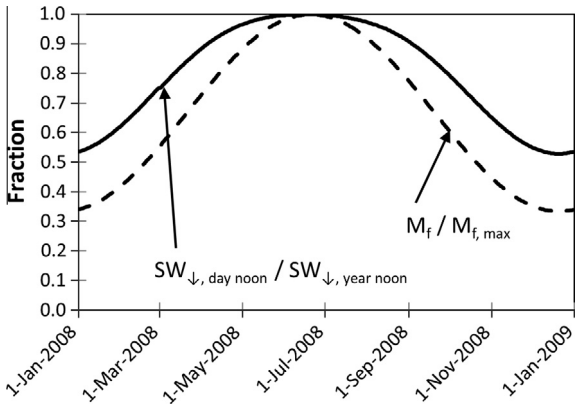

Fig. 4. Ratio of M_f to $M_{f,max}$ (used in TI model) compared to the ratio of $SW_{\downarrow,day\ noon}$ to $SW_{\downarrow,year\ noon}$ (used in RTI model). These ratios are used in their respective models to account for seasonal changes in the calculation of ΔD_t.

$K_{v,deciduous}$ and $K_{v,evergreen}$ was set to 0.4 based on USACE (1956) and an estimated 25% fractional vegetation cover in the forested areas of SBB. Due to the sparse and patchy vegetation in other land cover classifications as well as the tendency of snow to cover all vegetation except for trees in SBB, K_v for all other classifications was set to 1.0.

Recall that the original TI model partially accounted for seasonal changes to α and $SW_{\downarrow}$ by empirically varying M_f with time. Because both α and $SW_{\downarrow}$ are now incorporated into the RTI model and vary seasonally, M_f is assumed to remain constant in the RTI model. The original TI model uses the ratio of M_f to $M_{f,max}$ to indirectly account for seasonal changes in the calculation of ΔD_t (Eqs. (1) and (2)). Because M_f is constant in the RTI model, the RTI model instead accounts for seasonal changes in ΔD_t by replacing the previous ratio with the ratio of $SW_{\downarrow,day,noon}$ to $SW_{\downarrow,year,noon}$, where $SW_{\downarrow,day,noon}$ is the shortwave radiation at noon on a flat surface for the day of interest and $SW_{\downarrow,year,noon}$ is the maximum shortwave radiation at noon on a flat surface over the entire year. Calculation of $SW_{\downarrow,day,noon}$ and $SW_{\downarrow,year,noon}$ only requires S_0, K_s, K_r, and K_{atm}, which are already used by the RTI model. Using common values of 1.2 for $M_{f,max}$ and 0.4 for $M_{f,min}$ (Anderson, 2006), the ratios M_f /$M_{f,max}$ and $SW_{\downarrow,day\ noon}/SW_{\downarrow,year\ noon}$ are compared in Fig. 4 for SBB during the year 2008. Although not exact, the ratio of $SW_{\downarrow,day\ noon}/SW_{\downarrow,year\ noon}$ resembles the ratio of $M_f/M_{f,max}$, indicating that seasonal changes are still included in the calculation of ΔD_t within the RTI model. These modifications in the RTI model replace the need to calibrate both $M_{f,min}$ and $M_{f,max}$ with only M_f.

PEST indicates that the parameters related to melt factors are the most sensitive in both the TI ($M_{f,min}$ and $M_{f,max}$ parameters) and RTI (M_f parameter) simulations (Table 1). $K_{v,evergreen}$ in the RTI model calibrates to 1.000, essentially nullifying any reduction in shortwave radiation due to canopy cover from evergreen trees. The model is insensitive to $K_{v,deciduous}$ likely due to the relatively small area (0.3% of basin) that is classified as deciduous forest, and $K_{v,deciduous}$ calibrates to a value of 0.400 (the starting value).

4. Results and discussion

The results of the TI and RTI models were analyzed in three ways: (1) comparison to observations at SASP and SBSP, (2) comparison of SWE at four selected locations with similar elevations but differences in aspect and vegetation cover, and (3) comparison of SCA and SWE patterns over the entire basin.

4.1. SASP and SBSP

One way to partially test the RTI model is to compare its estimates of $SW_{\downarrow}$ and $LW_{\downarrow}$ to the observations at the SASP and SBSP sites. When calculating $SW_{\downarrow}$ at these sites, K_v was set to 1.0, which indicates no vegetation shading. K_s was calculated under the assumption that the pyranometers are level. No parameters were calibrated in the calculation of $SW_{\downarrow}$ or $LW_{\downarrow}$ at these sites, so the calibration and validation periods can be considered together. All comparisons of $SW_{\downarrow}$ and $LW_{\downarrow}$ are made using hourly observation and simulation data.

Fig. 5 shows the simulated and observed $SW_{\downarrow}$ and $LW_{\downarrow}$ over a representative 7-day span in April 2011. The timing of the rise and fall of $SW_{\downarrow}$ over the day is mostly well captured for the days in this period. However, on cloud-free days (2nd and 3rd days), the model underestimates $SW_{\downarrow}$ by approximately 10%. On the other days when clouds are present, the model both underestimates and overestimates $SW_{\downarrow}$. The observed $LW_{\downarrow}$ values change little in comparison with $SW_{\downarrow}$, but higher values correspond to periods with clouds. The model tends to overestimate $LW_{\downarrow}$ during cloud-free days and underestimate when clouds are present.

Considering $SW_{\downarrow}$ for the entire simulation, the Nash–Sutcliffe Efficiency (Nash and Sutcliffe, 1970) is 0.80 for both SASP and SBSP, which suggests that the errors in the $SW_{\downarrow}$ estimates are rather small relative to the variability of the observed $SW_{\downarrow}$ values. These high efficiency values likely occur because the model continues to estimate the timing of the rise and fall in $SW_{\downarrow}$ quite well in each day. The root mean squared error (RMSE) is 133 W m^{-2} for SASP and 129 W m^{-2} for SBSP. At SASP, the RMSE is approximately 64% of the average observed $SW_{\downarrow}$ and 10% of the peak observed $SW_{\downarrow}$. At SBSP, the RMSE is approximately 61% of the average observed $SW_{\downarrow}$ and 10% of the peak observed $SW_{\downarrow}$. The RTI model tends to overestimate values of $SW_{\downarrow}$ at both test plots with a mean bias error (MBE) of 12.4 W m^{-2} and 14.8 W m^{-2} at SASP and SBSP, respectively. These results imply that one or more of the reduction factors in Equation (13) are set too high (thus increasing $SW_{\downarrow}$). Among the reduction factors, K_{atm} is the most likely to be inaccurate because it was originally developed for agricultural purposes. A method described in Bras (1990) was also tested in which K_{atm} can be calculated based on a turbidity factor of the air and the solar elevation angle. This method produced similar accuracy but tended to underestimate $SW_{\downarrow}$ at both locations.

Comparisons between simulated and observed $LW_{\downarrow}$ are only made when snow is present. RMSE at SASP is 40.8 W m^{-2} (20% of the average observed $LW_{\downarrow}$) and 47.9 W m^{-2} at SBSP (22% of the average). MBE is 12.4 W m^{-2} at SASP and 21.2 W m^{-2} at SBSP, which are both approximately 10% of the average $LW_{\downarrow}$ at the respective gage. Cloud cover increases the simulated $LW_{\downarrow}$ up to 17% (Eq. (8)) with an average increase of 11%. Sicart et al. (2006) found in the Wolf Creek Research Basin in Canada that an increase of up to 50% in $LW_{\downarrow}$ could be attributed to clouds. However, those large increases were rare and average increases in $LW_{\downarrow}$ due to clouds was close to 16%, slightly higher than the 11% average increase found in this study. These results indicate that the approximate increase in $LW_{\downarrow}$ due to clouds may be accounted for in the TVA (1972) method, but the peak increases in $LW_{\downarrow}$ due to clouds may be absent and warrants further investigation. Bohn et al. (2013) indicated that other methods might estimate $LW_{\downarrow}$ better than the TVA (1972) method. Thus, a more complicated method by Crawford and Duchon (1999) was tested. The Crawford and Duchon (1999) method determines a cloud fraction term by calculating the ratio of measured solar irradiance to the clear-sky irradiance. In the absence of such data, Bohn et al. (2013) used the ratio of calculated solar irradiance to the clear-sky irradiance, which is the same as K_c as defined earlier. Using the cloud fraction term,

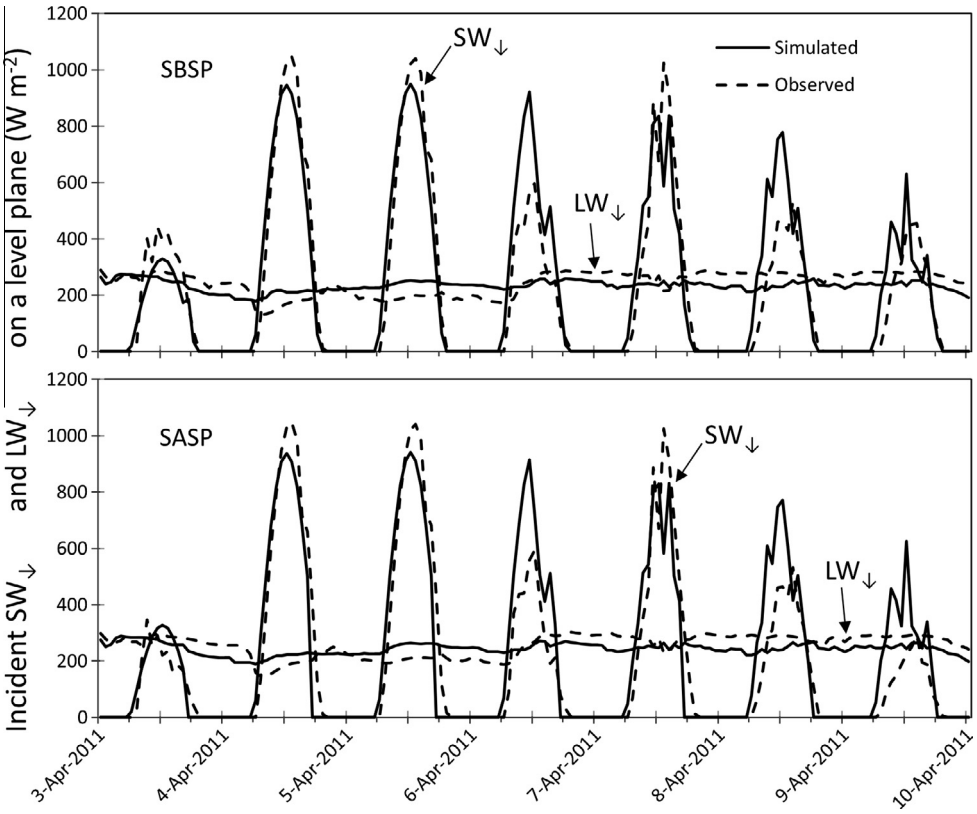

Fig. 5. Comparison of observed (dashed) and RTI simulated (solid) $SW_{\downarrow}$ and $LW_{\downarrow}$ at SBSP (top) and SASP (bottom) over a typical 7 day period in April 2011.

$LW_{\downarrow}$ was then calculated based on T_a and ε_a. When this method is implemented, the results at both SASP and SBSP have an increase in MBE of approximately 2.5 W m^{-2} and a decrease in RMSE of approximately 0.3 W m^{-2} when compared to the TVA (1972) method.

Fig. 6 shows the SWE values from the TI and RTI models at SBSP and SASP, and it compares them to the SWE observations and simulated values from the SNTHERM model, which were produced by Landry et al. (2014). Neither the TI or RTI models were calibrated to these SWE observations (they were calibrated to SCA), and the SNTHERM parameters were set to values commonly found in literature (Landry et al., 2014). At SBSP, the TI and RTI results tend to be similar to the SNTHERM results. However, at SASP, both models are more accurate than SNTHERM. At SBSP, RTI slightly

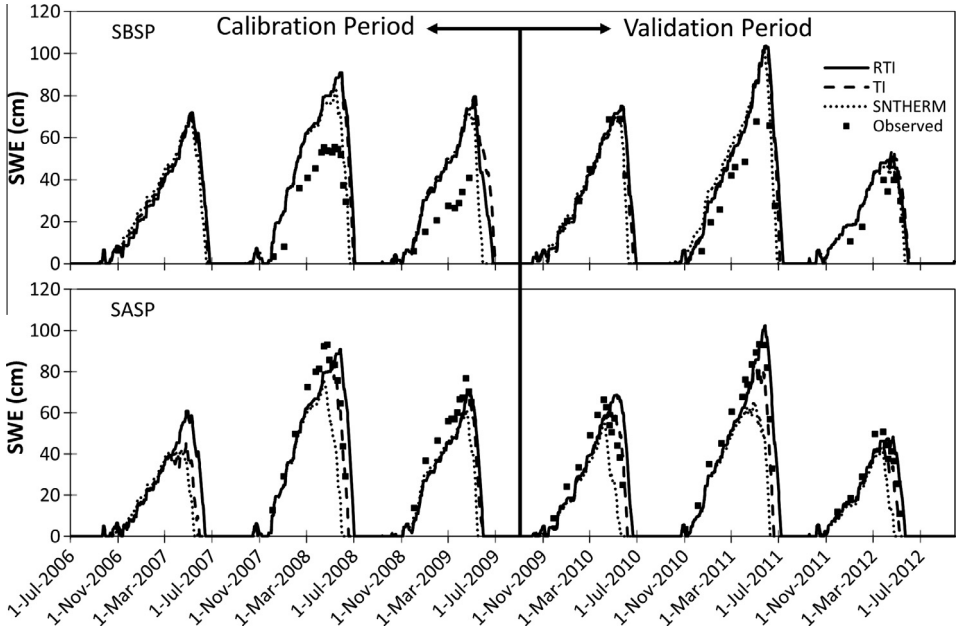

Fig. 6. TI and RTI simulated SWE at SBSP (top) and SASP (bottom) compared to observation data and published SNTHERM simulation results (Landry et al., 2014).

Table 2
Statistics for TI and RTI SWE values at SASP and SBSP during the calibration period (1 July 2006–30 September 2009), validation period (1 October 2009–30 September 2012), and overall (1 July 2006–30 September 2012). Values closer to zero indicate better fit.

	Calibration		Validation		Overall	
	RMSE (cm)	MBE (cm)	RMSE (cm)	MBE (cm)	RMSE (cm)	MBE (cm)
TI SBSP	26.6	24.0	14.0	10.5	21.1	17.4
RTI SBSP	26.6	23.8	13.7	10.0	21.1	17.0
TI SASP	8.8	−7.7	9.4	−5.7	9.1	−6.5
RTI SASP	14.5	−2.4	13.0	3.1	13.6	0.9

outperforms TI (i.e. its RMSE and MBE are the same or closer to zero, Table 2) during both the calibration and validation periods. At SASP, the TI model has smaller RMSE values while the RTI model has smaller (magnitude) MBE values during the calibration and validation periods.

In general, the TI and RTI results track closely together at both locations. The TI model tends to slightly underestimate the SWE at SASP (negative MBE values in Table 2) and overestimate the SWE at SBSP (positive MBE values in Table 2), while the RTI model tends to overestimate the SWE at both SASP and SBSP (positive overall MBE values in Table 2). Wind scour is estimated to reduce the maximum SWE by up to 40% at SBSP (Landry et al., 2014). Because the models do not represent this process, it might explain why they tend to overestimate SWE at SBSP. The SASP site is more sheltered, and the modeled results are closer to the observed SWE.

The importance of cloud cover in the RTI model was evaluated by comparing the behavior of the TI and RTI models for the periods with and without cloud cover data. For the five water years with cloud cover data, the peak SWE for the RTI model is on average 17.8% higher at SASP and 1.8% lower at SBSP when compared to the TI model. For the period with no cloud data (08 April 2009 through 11 November 2009), the peak SWE from the RTI model is approximately 1.2% higher at SASP and 2.1% lower at SBSP than the TI model. The simulations were repeated using the assumption that the sky was clear during the period without data. In that case, the RTI model is approximately 1.2% higher at SASP and 6.3% lower at SBSP. These differences in peak SWE (especially at SBSP) indicate that the assumption made for missing cloud cover data has significant impacts on the simulation of SWE in the RTI model. Cloud cover also appears to impact the simulated snowpack duration in the RTI model. At SBSP, the TI and RTI models completely melt the snowpack within a week of each other in every WY, with WY 2009 and WY 2012 being the only two years where snow depletion occurred in the RTI model prior to the TI model. At SASP, the RTI model tends to completely melt the snowpack later than the TI model (between thirteen and sixteen days). The exception is WY 2009 when cloud data were not completely available and the RTI and TI model completely melt the snowpack on the same day at SASP. This result also suggests that cloud cover impacts the simulation of SWE in the RTI model.

The impact of dust on SWE is not accounted for in either the RTI or TI model. Skiles et al. (2015) showed an increasing trend in the number of dust events (occurring between March 1st and snow depletion for each calendar year) from 2006 through 2012 at SASP. However, the number of dust events is not a predictor of the amount of dust deposited within a basin (Skiles et al., 2015). Dust concentration (measured just prior to snow depletion) was relatively similar between the calibration and validation periods (ranging from 0.8 to 1.3 mg g^{-1}) for all years except 2009 and 2010, which both experienced greater than 4.0 mg g^{-1} of dust concentration. Of the years analyzed, the observed recession of the SWE for WY 2010 at SASP is quicker than that of the TI or RTI simulations (note that SWE measurements during snow recession are lacking in WY 2009). The rapid recession in observed SWE when compared to simulated SWE is likely caused by the high concentration of dust during WY 2010. Future work could include the impact of dust in the RTI model by modifying the snow albedo (α).

4.2. Locations varying in aspect and vegetation cover

Simulations of SWE at SBSP and SASP yielded very similar results between the TI and RTI models. However, these sites are flat with relatively low vegetation cover. Greater differences in SWE are expected when the topography and vegetation cover play larger roles. To evaluate the sensitivity of the models to these factors, the SWE values from the TI and RTI models were compared for four locations within the basin (locations shown in Fig. 3). The four sites were chosen to have similar elevations (between 3493.1 and 3511.4 m), but they have strong differences in their topographic orientation (north-facing vs. south-facing) and their vegetation cover (evergreen forest vs. grassland or bare ground). No further calibration or additional simulations were performed for this analysis; it simply considers other locations in the watershed.

The SWE simulated by the TI model is nearly identical at the four locations (maximum difference of 1.8 cm) because this model does not account for topographic aspect and vegetation cover and the elevation differences between the sites are small. For clarity, a single representative result from the TI model is shown in Fig. 7. In contrast, the SWE simulated by the RTI model varies for the four locations. Both north-facing locations typically exhibit higher values of SWE than the TI model throughout the entire simulation due to a reduction in $SW_{\downarrow}$ caused by K_s. The same factor causes the south-facing locations to exhibit lower values of SWE than the TI model. These results demonstrate that the topographic orientation plays a strong role in determining the SWE pattern for mountainous terrain in the RTI model, while this factor is neglected in the TI model.

For both the north-facing and south-facing slopes the forested locations consistently have lower SWE values than the non-forested locations. Differences in SWE due to the forest canopy were caused solely by an increase in $LW_{\downarrow}$ due to the canopy (recall that $T_{canopy} = T_a$ and the emissivity between the canopy and the snow surface, ε_c, is equal to unity for forested areas). The values of K_v were set or calibrated to 1.0 (except for a small portion of deciduous forest), causing no decrease in $SW_{\downarrow}$ due to the canopy cover. No data are available in SBB to determine if snow persists longer in the open or forested areas, but Lundquist et al. (2013) found that snow typically persists longer under the canopy than in the open areas for areas with colder winters. If the K_v values were set lower than unity, $SW_{\downarrow}$ would be reduced under the canopy and snow would persist longer at such locations.

4.3. Snow cover area

Figs. 8 and 9 show the LandSat-derived SCA maps along with the SWE maps produced by the TI and RTI models. The 6 images in Fig. 8 show the maps from the calibration period, and the remaining 6 images in Fig. 9 show the maps from the validation

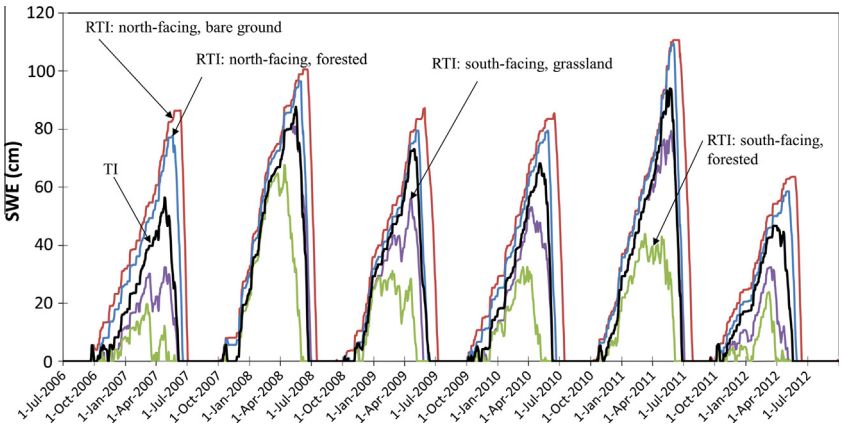

Fig. 7. SWE simulation at four locations within SBB that have similar elevations (between 3493.1 and 3511.4 m), but vary in aspect and vegetation cover. The TI model (black) simulates all four sites nearly identically, but the RTI model (colored) simulates each site differently. (For interpretation of the references to color in this figure legend, the reader is referred to the web version of this article.)

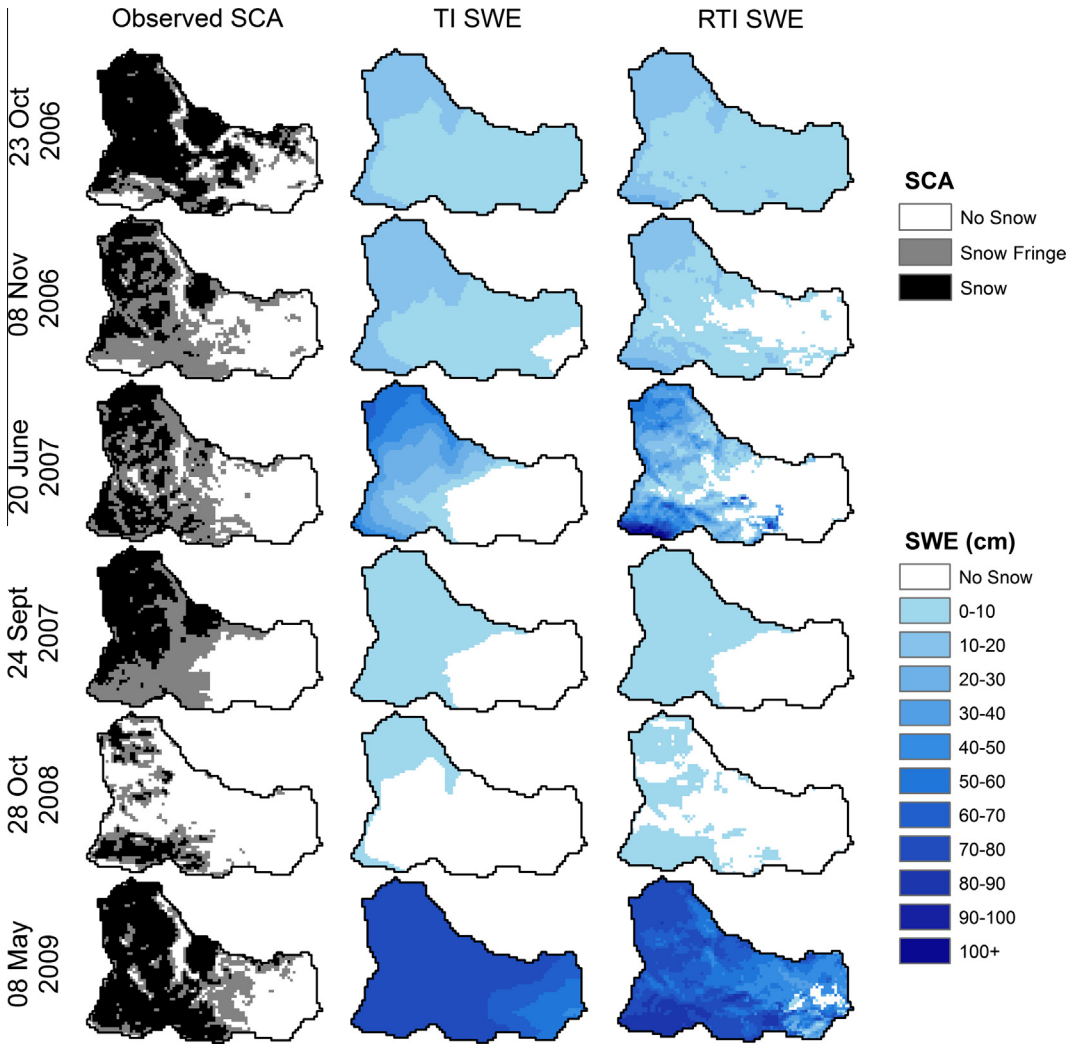

Fig. 8. Basin-wide observed SCA (left, from LandSat 5 imagery), and TI (center) and RTI (right) simulated SWE from the calibration period (1 July 2006–30 September 2009).

period. The spatial variation in the TI SWE map is only due to variations in elevation, which is used to derive the local T_a. In contrast, the spatial variation in the RTI SWE map depends on elevation, topographic-orientation, and (to a small extent) vegetation cover because they affect T_{rad}. All of the images in Figs. 8 and 9 show that there is a clear distinction in how the TI and RTI models simulate spatial patterns of SWE. Qualitatively, the RTI model typically outperforms the TI model in reproducing SCA (e.g., 20 June 2007 and 21 October 2011). Skiles et al. (2015) found that dust deposition at SASP advanced melt by 24–49 days. Including dust in the calcu-

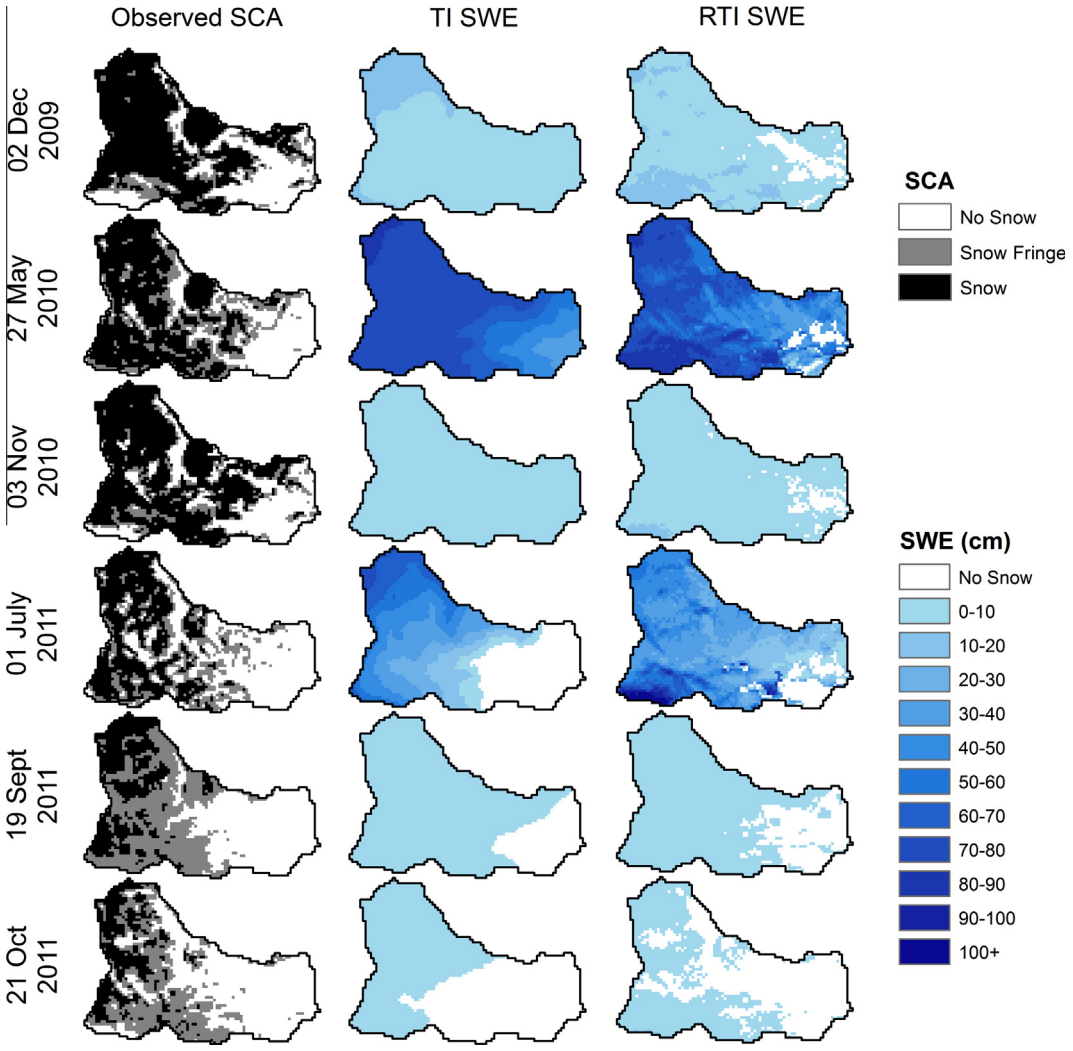

Fig. 9. Basin-wide observed SCA (left, from LandSat 5 imagery), and TI (center) and RTI (right) simulated SWE from the validation period (1 October 2009–30 September 2012).

lation of α in the RTI model could potentially improve SCA simulations at SBB during the ablation period (note overestimation of SCA for 08 May 2009 and 27 May 2010 and recall that both years had high dust concentration (Skiles et al., 2015)).

For the TI simulation, the average error (Eq. (20)) is 0.44 during the calibration period, 0.40 during the validation period, and 0.42 overall. For the RTI simulation, the average error is 0.29 during the calibration period, 0.36 during the validation period, and 0.33 overall. Of the 12 observation dates, the TI and RTI models produced the same error for 2 images (23 October 2006 and 24 September 2007, both in calibration period), the RTI model had higher error for 1 image (01 July 2011, in validation period), and the RTI model had a lower error for 9 images (4 in calibration period, 5 in validation period). The simulations of SCA were also evaluated using the F score as described in Rittger et al. (2013). The F scores tend to be better for the RTI patterns (average of 0.86) than the TI patterns (average of 0.80), and the F scores also suggest that the RTI SCA is superior for 9 of the 12 observation dates.

Fig. 10 analyzes the composition of the error in SCA for each image. Specifically, it shows the percent of the basin where: (1) snow was observed and simulated (accurately simulated snow), (2) snow was not observed and not simulated (accurately simulated no snow), (3) snow was observed but was not simulated (under-simulated snow), and (4) snow was not observed but was simulated (over-simulated snow). During the calibration period, the model was calibrated to minimize the contributions of (3) and (4); cases (1) and (2) represent the accuracy of the models. The average SCA accuracy modestly improves from 75.5% for the TI model to 79.9% for the RTI model with a maximum improvement of 19.7% on 28 October 2008 followed by a 14.0% improvement on 8 November 2006. Both the TI and RTI models have higher average accuracies for the calibration period (76.6% and 82.9%, respectively) than the validation period (74.4% and 76.9%, respectively). The improved performance suggests that the RTI model captures some elements of the snowpack evolution that are not included in the TI model. The improvement may be small in part because the RTI introduces much more local variation in the SWE pattern than the TI model.

4.4. Basin-wide SWE volume

Basin-wide SWE is often calculated to help plan water allocations and reservoir management. Although no basin-wide SWE observations are available, it is useful to see whether the TI and RTI model produce substantial differences in this quantity. The total volume of SWE (m^3) as a function of time during the simulations is shown in Fig. 11 for both the TI and RTI models. During the accumulation periods, both models estimate very similar volumes

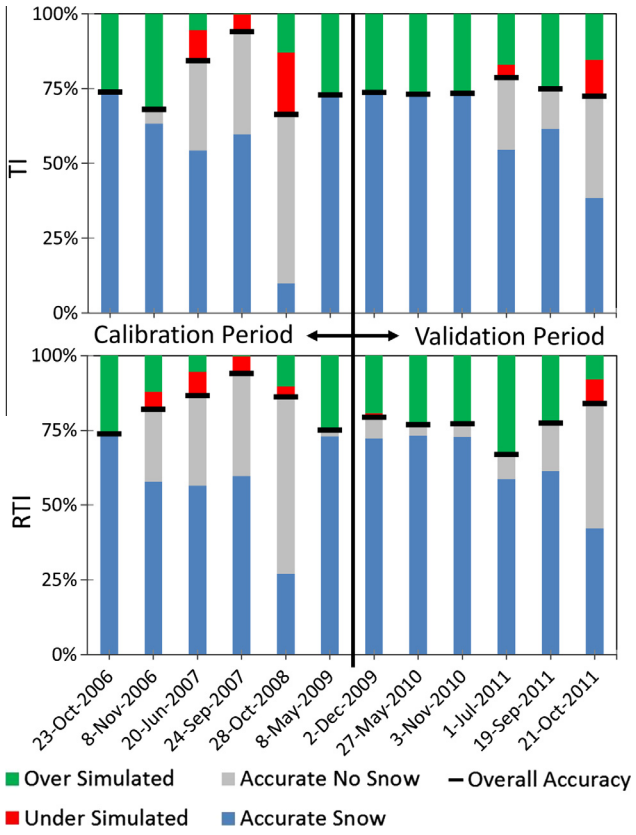

Fig. 10. Composition of the SCA from the TI model (top) and RTI model (bottom) as percentages of total basin area. The heights of the black lines indicate the accuracy of the SCA on each date.

of SWE. This similarity continues until just prior to the peak in each WY. As melting begins, the TI estimates are typically higher than the RTI estimates. The differences are especially large during the melting period of WY 2009 when the cloud cover was estimated. The difference in the annual peak SWE varied from 53,831 m^3 (2.1% difference) in WY 2008 to a 260,168 m^3 (12.9%) difference in WY 2007. The largest percentage difference occurred in WY 2012 with the RTI model simulating 13.9% (209,268 m^3) less SWE than TI. On average, the annual peak SWE was 187,579 m^3 greater for the TI model than the RTI model (an 8.5% difference). The snowpack completely disappeared in every WY for both the TI and RTI models. Snow in the RTI model disappeared between 8 days (WY 2012) and 37 days (WY 2010) after snow had disappeared in the TI model. This delay (an average of 21.5 days) was caused in part by snow remaining in a few high-elevation topographically-shaded areas within the RTI model.

5. Conclusions

This study aimed to better account for the energy that is available to heat or melt snowpack in the GSSHA snowpack routine. The existing TI model uses air temperature as a proxy for the available energy because measurements for this variable are widely available. However, air temperature is most directly related to the longwave radiation from the air (Ohmura, 2001), which is only one contributor in the energy balance. We proposed to replace the air temperature with an alternative proxy, which is calculated from a simple radiation balance. This new RTI model retains the general structure of the TI approach and requires only one additional type of data (cloud cover). The RTI model also includes an estimate of the absorbed shortwave radiation, which is often the dominant source of energy for snow melt (Sicart et al., 2006; DeWalle and Rango, 2008), and it includes the effects of topographic orientation and vegetation cover. Because shortwave radiation is directly considered in the RTI model, two calibrated melt factor terms in the TI model can be replaced with a single melt factor term. To account for vegetation effects, the RTI model does require two inputs related to vegetation: the vegetation transmission coefficient and the leaf area index. However, both of these inputs are currently used in the evapotranspiration routine of GSSHA. Because the RTI model retains the general structure of the TI model, it can easily be implemented into existing distributed models that use the TI model.

In this study, the RTI model was applied to the SBB and compared to local observations of SWE and LandSat-derived maps of SCA. Its results were also compared to the TI model and, at the local scale, to those of the SNTHERM model. The primary conclusions of the paper are as follows:

(1) When the TI and RTI models are calibrated to basin-wide SCA and then applied to the SBSP and SASP sites, they produce similar performance. For example, when compared to observed SWE data, the RTI model has a lower MBE at both sites than the TI model, but a larger RMSE at SASP. Both models perform better at SASP than SBSP, which has known effects from wind scour that are not accounted for in the

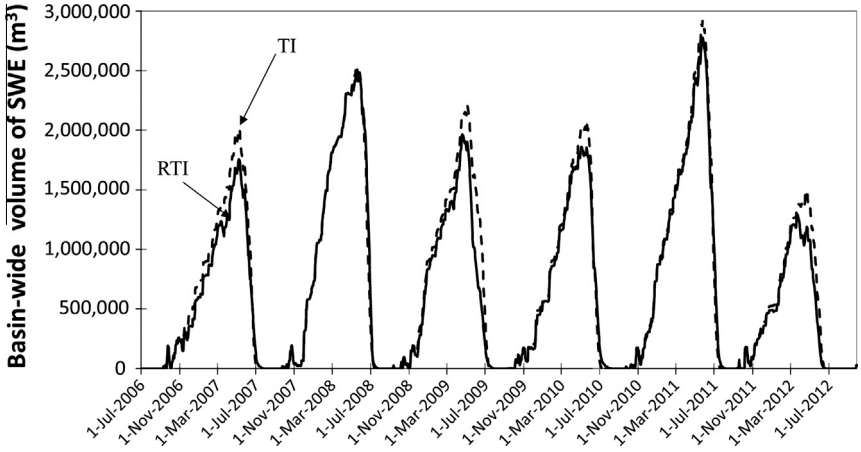

Fig. 11. Basin-wide volume of SWE (m^3) simulated by the TI model (dashed) and the RTI model (solid) during the entire study period. Cloud cover was assumed to be absent in the RTI model from 08 April 2009 through 11 November 2009 due to the lack of cloud cover data.

models. These sites both have little slope and low vegetation cover, so the elements that distinguish the TI and RTI models have little effect. Both methods outperform published results from an uncalibrated SNTHERM model for these sites and produce reasonable estimates of the observed SWE. Thus, at least for this basin, the RTI model appears to have similar performance as the TI model for flat and thinly vegetated locations.

(2) The RTI model produces substantial variations in SWE depending on the topographic orientation and vegetation cover whereas the TI model does not. The RTI model includes the effect of the topographic orientation in its calculation of the absorbed shortwave radiation and thus its proxy temperature. North-facing slopes tend to have more SWE than south-facing slopes. Similarly, when forested and non-forested locations are compared, the non-forested locations have more SWE than the forested locations due to enhanced longwave radiation from the forest cover. The differences between the forested and non-forested locations are expected to be specific to this watershed, and the RTI model likely requires additional data to ensure accurate representation of these differences. In contrast, the TI model infers its proxy temperature using only elevation and thus exhibits no variations based on topographic orientation or vegetation cover.

(3) The basin-wide SCA area maps from the RTI model are typically more accurate than those from the TI model at SBB, showing improved accuracy in 9 of the 12 images analyzed, similar accuracy in 2 images, and reducing the error from 0.42 to 0.33. The F score (Rittger et al., 2013) modestly improved from 0.8 to 0.86 when using the RTI model. The RTI model's dependence on topographic orientation and vegetation cover produce more local variability in SWE than the TI model. These local variations resemble the variability in SCA maps that are derived from LandSat images. In contrast, the TI model produces very smooth SWE maps that depend only on elevation and often do not resemble the SCA maps from LandSat.

(4) The differences between the TI and RTI models produce substantial differences in the overall volume of SWE in the study basin. The peak basin-wide SWE value in a given water year is 2.1% to 13.9% smaller for the RTI model than the TI model, which could impact water allocation and reservoir operation plans. Although observations are not available to determine which estimate is more accurate, this result suggests that the differences in the TI and RTI models are significant and deserve further testing.

(5) Cloud cover can have a significant effect on the estimation of both shortwave radiation and SWE within the RTI model. During the WY 2009 melting period, cloud cover data were unavailable and therefore estimated hourly by randomly sampling the values from the same day and hour of the other years. This assumption resulted in expedited melting of the snowpack in the RTI model compared to the TI model. It is unclear whether the RTI model can be effectively deployed in basins without observed cloud cover data (perhaps by manipulating calibration parameters such as the melt factor, by calibrating the cloud cover fraction, or using remotely-sensed cloud cover products). Without cloud cover data, the RTI model still accounts for the effects of topography and vegetation on shortwave radiation and SWE, but its performance is likely diminished.

Additional testing is needed to better characterize the differences between the TI and RTI models. The present study revealed that the most considerable differences occur in locations with substantial topographic and vegetation effects. Future research should focus on comparing to observations in such locations to determine the relative reliability of the two methods. In addition, future testing could determine the magnitude to topographic and vegetation variations that are needed to produce substantial differences between the two methods. Additional testing should also consider the role of cloud cover in more detail. Performance of the RTI model might differ for areas with cloudier climates, such as the Pacific Northwest. Similarly, the performance of the RTI model in basins dominated by turbulent fluxes (e.g., warm temperate mountain climates (Sade et al., 2014)) may be diminished and should be studied. The RTI model also neglects the effects of dust, wind scour, and emission of longwave radiation from local topography; all of which may cause errors in the simulation of SWE and SCA. Dust could be included through a more detailed calculation of snow albedo. Future testing should also examine the performance of the RTI model at predicting the overall volume of SWE in the watershed as well as the timing and magnitude of snowmelt discharges in the spring.

Acknowledgements

This project was funded by the Flood and Coastal Research Program at the U.S. Army Corps of Engineers, Engineering Research and Development Center, Coastal and Hydraulics Laboratory in Vicksburg, Mississippi. We also thank three anonymous reviewers who provided helpful comments that substantially improved this article.

References

Aguado, E., 1985. Radiation balances of melting snow covers at an open site in the Central Sierra Nevada, California. Water Resour. Res. 21 (11), 1649–1654.
Allen, R.G., Walter, I.A., Elliott, R., Howell, T., Itenfisu, D., Jensen, M., 2005. The ASCE Standardized Reference Evapotranspiration Equation. ASCE.
Anderson, E.A., 1973. National Weather Service River Forecast System – Snow Accumulation and Ablation Model. Technical Memorandum NWS Hydro-17, November 1973. 217 pp.
Anderson, E.A., 1976. A Point of Energy and Mass Balance Model of Snow Cover. U.S. National Oceanic and Atmospheric Administration NOAA Technical Report NWS 19, Silver Spring, MD.
Anderson, E.A., 2006. Snow Accumulation and Ablation Model – SNOW-17, NWSRFS User Documentation. U.S. National Weather Service, Silver Springs, MD. <http://www.nws.noaa.gov/oh/hrl/nwsrfs/users_manual/part2/_pdf/22snow17.pdf>.
Aquaveo, 2013. Watershed Modeling System Version 9.1.4, Provo, UT.
Ball, G.H., Hall, D.J., 1965. ISODATA, a novel method of data analysis and pattern classification, DTIC Document.
Barrett, A.P., 2003. National Operational Hydrologic Remote Sensing Center Snow Data Assimilation System (SNODAS) Products at NSIDC. National Snow and Ice Data Center, Cooperative Institute for Research in Environmental Sciences.
Barros, A.P., Lettenmaier, D.P., 1993. Dynamic modeling of the spatial distribution of precipitation in remote mountainous areas. Mon. Weather Rev. 121 (4), 1195–1214.
Blöschl, G., Kirnbauer, R., Gutknecht, D., 1991. Distributed snowmelt simulations in an alpine catchment: 1. Model evaluation on the basis of snow cover patterns. Water Resour. Res. 27 (12), 3171–3179.
Bohn, T.J., Livneh, B., Oyler, J.W., Running, S.W., Nijssen, B., Lettenmaier, D.P., 2013. Global evaluation of MTCLIM and related algorithms for forcing of ecological and hydrological models. Agric. For. Meteorol. 176, 38–49.
Bookhagen, B., Burbank, D.W., 2010. Toward a complete Himalayan hydrological budget: spatiotemporal distribution of snowmelt and rainfall and their impact on river discharge. J. Geophys. Res. 115, F03019. http://dx.doi.org/10.1029/2009JF001426.
Bras, R.L., 1990. Hydrology: An Introduction to Hydrologic Science. Addison-Wesley, Reading, Massachusetts, 643 p.
Brubaker, K., Rango, A., Kustas, W., 1996. Incorporating radiation inputs into the snowmelt runoff model. Hydrol. Process. 10 (10), 1329–1343.
Butcher, P.J., 2009. Incorporating Radiation Inputs into an Operational Snowmelt Model. Graduate Theses and Dissertations, Paper 10694, Iowa State University, Ames, IA.
Carroll, T., Cline, D., Fall, G., Nilsson, A., Li, L., Rost, A., 2001. NOHRSC operations and the simulation of snow cover properties for the conterminous US. In: Proceedings of the 69th Annual Western Snow Conference, April 2001, Sun Valley, ID.
Cazorzi, F., Dalla Fontana, G., 1996. Snowmelt modelling by combining air temperature and a distributed radiation index. J. Hydrol. 181 (1–4), 169–187.

Crawford, T.M., Duchon, C.E., 1999. An improved parameterization for estimating effective atmospheric emissivity for use in calculating daytime downwelling longwave radiation. J. Appl. Meteorol. 38, 474–480.
Daly, S., Davis, R., Ochs, E., Pangburn, T., 2000. An approach to spatially distributed snow modelling of the Sacramento and San Joaquin basins, California. Hydrol. Process. 14 (18), 3257–3271.
DeWalle, D.R., Rango, A., 2008. Principles of Snow Hydrology. Cambridge University Press.
Doherty, J., Brebber, L., Whyte, P., 1994. PEST: Model-Independent Parameter Estimation. Watermark Computing, Corinda, Australia, 122.
Downer, C.W., Ogden, F.L., 2004. GSSHA: Model to simulate diverse stream flow producing processes. J. Hydrol. Eng. 9 (3), 161–174.
Downer, C.W., Ogden, F.L., 2006. Gridded Surface Subsurface Hydrologic Analysis (GSSHA) User's Manual; Version 1.43 for Watershed Modeling system 6.1 (No. ERDC/CHL-SR-06-1). Engineer Research and Development Center, Coastal and Hydraulics Laboratory, Vickburg, MS.
Downer, C.W., Ogden, F.L., Niedzialek, J.M., Liu, S., 2006. Gridded Surface/Subsurface Hydrologic Analysis (GSSHA) model: a model for simulating diverse streamflow producing processes. In: Singh, V.P., Frevert, D.K. (Eds.), Watershed Models. Taylor & Francis, CRC Press, Boca Raton, FL, pp. 131–157.
Dozier, J., Marks, D., 1987. Snow mapping and classification from Landsat Thematic Mapper data. Ann. Glaciol. 9 (1), 97–103.
Duffie, J.A., Beckman, W.A., 1980. Solar Engineering of Thermal Processes. Wiley, New York.
Dunn, S., Colohan, R., 1999. Developing the snow component of a distributed hydrological model: a step-wise approach based on multi-objective analysis. J. Hydrol. 223 (1), 1–16.
Eagleson, P.S., 1970. Dynamic Hydrology. McGraw-Hill, New York.
ERDAS, I., 1999. ERDAS Field Guide. Atlanta, Georgia, 672: p. 94.
Essery, R., Rutter, N., Pomeroy, J., Baxter, R., Stähli, M., Gustafsson, D., Barr, A., Bartlett, P., Elder, K., 2009. SnowMIP2: an evaluation of forest snow process simulations. Bull. Am. Meteorol. Soc. 90 (8), 1120–1135.
Etchevers, P., Martin, E., Brown, R., Fierz, C., Lejeune, Y., Bazile, E., Boone, A., Dai, Y.-J., Essery, R., Fernandez, A., Gusev, Y., Jordan, R., Koren, V., Kowalczyk, E., Nasonova, N.O., Pyles, R.D., Schlosser, A., Shmakin, A.B., Smirnova, T.G., Strasser, U., Verseghy, D., Yamazaki, T., Yang, Z.-L., 2004. Validation of the energy budget of an alpine snowpack simulated by several snow models (SnowMIP project). Ann. Glaciol. 38 (1), 150–158.
Follum, M.L., Downer, C.W., 2013. Snow Water Equivalent Modeling Capabilities of the GSSHA Watershed Model. U.S. Army Corps of Engineers, Coastal and Hydraulic Laboratory Technical Report 13–4, Vicksburg, MS.
Franz, K.J., Hogue, T.S., Sooroshian, S., 2008. Operational snow modeling: addressing the challenges of an energy balance model for National Weather Service forecasts. J. Hydrol. 360 (1), 48–66.
Fry, J.A., Xian, G., Jin, S., Dewitz, J.A., Homer, C.G., Limin, Y., Barnews, C.A., Helold, N. D., Wickham, J.D., 2011. Completion of the 2006 national land cover database for the conterminous United States. Photogramm. Eng. Rem. Sens. 77 (9), 858–864.
Gerdel, R.W., 1954. The transmission of water through snow. Trans. Am. Geophys. Union 35 (3), 475–485.
Gesch, D., Oimoen, M., Greenlee, S., Nelson, C., Steuck, M., Tyler, D., 2002. The national elevation dataset. Photogramm. Eng. Rem. Sens. 68 (1), 5–32.
Henneman, H.E., Stefan, H.G., 1999. Albedo models for snow and ice on a freshwater lake. Cold Reg. Sci. Technol. 29 (1), 31–48.
Hock, R., 1999. A distributed temperature-index ice-and snowmelt model including potential direct solar radiation. J. Glaciol. 45 (149), 101–111.
Hock, R., 2003. Temperature index melt modelling in mountain areas. J. Hydrol. 282 (1–4), 104–115.
Idso, S.B., 1981. A set of equations for full spectrum and 8- to 14-μm and 10.5- to 12.5-μm thermal radiation from cloudless skies. Water Resour. Res. 17 (2), 295–304.
Jordan, R., 1991. A One-Dimensional Temperature Model for a Snow Cover: Technical Documentation for SNTHERM.89. U.S. Army Corps of Engineers, Cold Regions Research and Engineering Laboratory, Hanover, NH.
Jost, G., Weiler, M., Gluns, D.R., Alila, Y., 2007. The influence of forest and topography on snow accumulation and melt at the watershed-scale. J. Hydrol. 347 (1), 101–115.
Jost, G., Moore, R., Smith, R., Gluns, D., 2012. Distributed temperature-index snowmelt modelling for forested catchments. J. Hydrol. 420–421, 87–101.
Kang, D.H., 2005. Distributed Snowmelt Modeling with GIS and CASC2D at California Gulch, Colorado. Colorado State University, Fort Collins, CO, 195 p.
Kirnbauer, R., Bloeschl, G., Gutknecht, D., 1994. Entering the era of distributed snow models. Nord. Hydrol. 25 (1), 1–24.
Kumar, M., Marks, D., Dozier, J., Reba, M., Winstral, A., 2013. Evaluation of distributed hydrologic impacts of temperature-index and energy-based snow models. Adv. Water Resour. 56, 77–89.
Kustas, W.P., Rango, A., Uijlenhoet, R., 1994. A simple energy budget algorithm for the snowmelt runoff model. Water Resour. Res. 30 (5), 1515–1527.
Landry, C.C., Buck, K.A., Raleigh, M.S., Clark, M.P., 2014. Mountain system monitoring at Senator Beck Basin, San Juan Mountains, Colorado: a new integrative data source to develop and evaluate models of snow and hydrologic processes. Water Resour. Res. 50 (2), 1773–1788.
Lei, F., Koren, V., Smith, M., Moreda, F., 2007. A sensitivity study of an energy budget snow accumulation and ablation model. In: Paper J.6.4. American Meteorological Society, San Antonio, TX.
Liou, K.N., 2002. An Introduction to Atmospheric Radiation, second ed. Academic Press, New York.
Liston, G.E., Elder, K., 2006. A distributed snow-evolution modeling system (SnowModel). J. Hydrometeorol. 7 (6), 1259–1276.
Luce, C.H., Tarboton, D.G., Cooley, K.R., 1998. The influence of the spatial distribution of snow on basin-averaged snowmelt. Hydrol. Process. 12 (1011), 1671–1683.
Lundquist, J.D., Dickerson-Lange, S.E., Lutz, J.A., Cristea, N.C., 2013. Lower forest density enhances snow retention in regions with warmer winters: a global framework developed from plot-scale observations and modeling. Water Resour. Res. 49 (10), 6356–6370.
Mhawej, M., Faour, R., Fayad, A., Shaban, A., 2014. Towards an enhanced method to map snow cover areas and derive snow-water equivalent in Lebanon. J. Hydrol. 513, 274–282.
Molotch, N.P., Bales, R.C., 2006. Comparison of ground-based and airborne snow surface albedo parameterizations in an alpine watershed: impacts on snowpack mass balance. Water Resour. Res. 42 (5), WR05410. http://dx.doi.org/10.1029/2005WR004522.
Nash, J.E., Sutcliffe, J.V., 1970. River flow forecasting through conceptual models. Part I – A discussion of principles. J. Hydrol. 10 (3), 282–290.
Ohmura, A., 2001. Physical basis for the temperature-based melt index method. J. Appl. Meteorol. 40, 753–761.
Painter, T.H., Barrett, A.P., Landry, C.C., Neff, J.C., Cassidy, M.P., Lawrence, C.R., McBride, K.E., Lang, G., 2007. Impact of disturbed desert soils on duration of mountain snow cover. Geophys. Res. Lett. 34 (12).
Pomeroy, J., Gray, D., Hedstrom, N., Janowicz, J., 2002. Prediction of seasonal snow accumulation in cold climate forests. Hydrol. Process. 16 (18), 3543–3558.
Pomeroy, J.W., Marks, D., Link, T., Ellis, C., Hardy, J., Rowlands, A., Granger, R., 2009. The impact of coniferous forest temperature on incoming longwave radiation to melting snow. Hydrol. Process. 23 (17), 2513–2525.
Prata, A.J., 1996. A new long-wave formula for estimating downward clear-sky radiation at the surface. Quart. J. Roy. Meteorol. Soc. 122 (533), 1127–1151.
Rittger, K., Painter, T.H., Dozier, J., 2013. Assessment of methods for mapping snow cover from MODIS. Adv. Water Resour. 51, 367–380.
Sade, R., Rimmer, A., Litaor, M.I., Shamir, E., Furman, A., 2014. Snow surface energy and mass balance in a warm temperate climate mountain. J. Hydrol. 519, 848–862.
Shamir, E., Georgakakos, K.P., 2006. Distributed snow accumulation and ablation modeling in the American River basin. Adv. Water Resour. 29 (4), 558–570.
Sharif, H.A., Sparks, L., Hassan, A.A., Zeitler, J., Xie, H., 2010. Application of a distributed hydrologic model to the November 17, 2004, Flood of Bull Creek Watershed, Austin, Texas. J. Hydrol. Eng. 15 (8), 651–657.
Shuttleworth, W.J., 1993. Evaporation. In: Maidment, D.R. (Ed.), Handbook of Hydrology. McGraw-Hill Inc., New York, pp. 4.6–4.31.
Sicart, J.E., Pomeroy, J.W., Essery, R.L.H., Bewley, D., 2006. Incoming lonwave radiation to melting snow: observations, sensitivity and estimation in northern environments. Hydrol. Process. 20, 3697–3708.
Sicart, J.E., Pomeroy, J.W., Essery, R.L.H., Hardy, J., Link, T., Marks, D., 2004. A sensitivity study of daytime net radiation during snowmelt to forest canopy and atmospheric conditions. J. Hydrometeorol. 5, 774–784.
Singh, P., Spitzbart, G., Hübl, H., Weinmeister, H.W., 1997. Hydrological response of snowpack under rain-on-snow events: a field study. J. Hydrol. 202 (1), 1–20.
Skiles, S.M., Painter, T.H., Deems, J.S., Bryant, A.C., Landry, C.C., 2012. Dust radiative forcing in snow of the Upper Colorado River basin: 2. Interannual variability in radiative forcing and snowmelt rates. Water Resour. Res. 48 (7), W07522.
Skiles, S.M., Painter, T.H., Belnap, J., Holland, L., Reynolds, R.L., Goldstein, H.L., Lin, J., 2015. Regional variability in dust-on-snow processes and impacts in the Upper Colorado River basin. Hydrol. Process. http://dx.doi.org/10.1002/hyp.10569.
Smith, J.A., 1993. Precipitation. In: Maidment, D.R. (Ed.), Handbook of Hydrology. McGraw-Hill Inc., New York, p. 3.4.
Tou, J.T., Gonzalez, R.C., 1974. Pattern recognition principles. Pattern Recogn. Phys., 1
TVA, 1972. Heat and Mass Transfer Between a Water Surface and the Atmosphere. Tennessee Valley Authority, Norris, TN.
USACE, 1956. Snow Hydrology, Summary Report of the Snow Investigations. U.S. Army Corps of Engineers, North Pacific Division, Portland, Oregon.
Vuyovich, C., Jacobs, J.M., 2011. Snowpack and runoff generation using AMSR-E passive microwave observations in the Upper Helmand Watershed, Afghanistan. Rem. Sens. Environ. 115 (12), 3313–3321.
Wahl, K., 1992. Evaluation of trends in runoff in the western United States. Managing Water Resour. Global Change, 701–710.
Wright, D.B., Smith, J.A., Baeck, M.L., 2014. Flood frequency analysis using radar rainfall fields and stochastic storm transposition. Water Resour. Res. 50 (2), 1592–1615.
Zanotti, F., Endrizzi, S., Bertoldi, G., Rigon, R., 2004. The GEOTOP snow module. Hydrol. Process. 18 (18), 3667–3679.
Zeinivand, H., De Smedt, F., 2009. Hydrological modeling of snow accumulation and melting on river basin scale. Water Resour. Manage 23, 2271–2287.